Transactions of Materials Research 1 (2025) 100011

Contents lists available at ScienceDirect

Transactions of Materials Research

journal homepage: www.sciencedirect.com/journal/transactions-of-materials-research

Comparative analysis of oxidation resistance at 1700 °C for HfB_2-SiC-$MoSi_2$ coatings on curved C/C composites prepared via gaseous and liquid silicon infiltration

Shubo Zhang, Zhiqiang Liu, Shuo Zhang, Xiaoxuan Su, Qiangang Fu *

Shanxi Key Laboratory of Fiber Reinforced Light Composite Materials, Science and Technology on Thermostructural Composite Materials Laboratory, Northwestern Polytechnical University, Xi'an, 710072, China

ARTICLE INFO

Keywords:
Silicon infiltration
Curved C/C composites
Oxidation
Coating

ABSTRACT

To investigate the differences in densification effects and oxidation resistance of curved samples subjected to gaseous and liquid Si infiltration, HfB_2-SiC-$MoSi_2$-Si/SiC-Si coated C/C composites are prepared using gaseous and liquid Si infiltration (G-HSM and L-HSM), respectively. The mass change rates of G-HSM and L-HSM after thermal shock from 1700 °C to room temperature are −2.52 % and 0.07 %. After isothermal oxidation at 1700 °C for 200 h, the mass change rate of L-HSM is −0.12 %, while that of G-HSM reaches −0.60 % after 124 h. The high content of HfB_2 and $MoSi_2$ in L-HSM improves the coating stability, which effectively avoids droplet shedding. In addition, the lower roughness and narrower original cracks reduce oxygen adsorption sites and diffusion channels of L-HSM during oxidation. Thus, L-HSM exhibits better thermal shock resistance and oxidation resistance than G-HSM. This study provides a strategy for the coating design of curved components above 1700 °C.

1. Introduction

As a key thermal structure component of an aero-engine, thin-walled and curved shaped components such as blades are proposed for increasingly demanding material properties [1,2]. Turbine blades not only have to withstand long-term high temperature oxidation near 1700 °C, but also need to resist high and low temperature alternation [1], which requires them to have excellent temperature-bearing performance in aerobic environment. Carbon/carbon (C/C) composites are promising among multitudinous high-temperature oxidation protection materials due to their high specific strength and modulus, low coefficient of thermal expansion and excellent stability of mechanical properties [3–8]. Unfortunately, carbon fibers and matrix are rapidly oxidized when exposed to an aerobic atmosphere above 370 °C, while it is difficult to resist their long-term oxidative corrosion, greatly limiting their applications in aerospace field [9–13].

Combining C/C composites with ultra-high-temperature ceramics (UHTCs) has become a promising solution to the problem of oxidation susceptibility of C/C composites [14–16]. Hf-based ceramic coatings, especially HfB_2-based coatings, are widely used for oxidation protection of C/C composites as their high melting point and excellent oxygen barrier [17,18]. However, B_2O_3 evaporates rapidly at over 1150 °C, forming a porous oxide layer of HfO_2 [19], which results in that a single HfB_2 system with pulverized oxidation cannot satisfy the demand for high-temperature and long-time oxidation protection. The introduction of SiC not only moderates the thermal expansion coefficient of UHTCs and C/C composites [20,21], but also helps to improve the stability of oxide film due to the good flowability of its oxidized product, SiO_2, which can heal defects in a timely manner at high temperatures [22,23]. In addition, $HfSiO_4$ generated from HfO_2 and SiO_2 further improves the high-temperature stability of the oxide film [17,24]. However, SiO_2 is susceptible to active oxidation at low oxygen partial pressures above 1600 °C to form SiO(g), resulting in the coating depletion [25]. Transition metal silicides can provide a silicon source and reduce silicon loss [26]. In particular, $MoSi_2$ has a suitable melting point (2030 °C) and good antioxidant properties [27–29]. Thereby, $MoSi_2$-modified HfB_2-SiC coatings are expected to realize the oxidation protection of C/C composites at 1700 °C.

Various methods have been successively developed to prepare the coating, such as slurry dipping, high temperature sintering and gaseous Si infiltration. Slurry dipping facilitates the design of the coating composition and structure, and is easy to apply on the surface of curved special-shaped components [30,31], but the porous structure formed by the buildup of raw slurry particles provides numerous channels for oxygen

* Corresponding author.
E-mail address: fuqiangang@nwpu.edu.cn (Q. Fu).

https://doi.org/10.1016/j.tramat.2025.100011
Received 23 March 2025; Received in revised form 6 April 2025; Accepted 6 April 2025
Available online 8 April 2025

intrusion [32]. High-temperature sintering, pre-oxidation and silicon infiltration are usually combined with slurry dipping to provide densification. Lv et al. [33] prepared HfB_2-SiC/SiC coatings on C/C surface through pack cementation, slurry painting and high-temperature reactive sintering, which could protect the substrate for 100 h at 1700 °C in air with a mass loss of 2.4 %. Zhu et al. [20] used pack cementation, slurry dipping and oxidative sintering to fabricate $HfSi_2$-HfB_2-SiC coatings, which protected C/C composites at 1200 °C, 1500 °C and 1700 °C for 516 h, 744 h and 64 h, respectively. Nevertheless, high-temperature sintering and pre-oxidation can only densify local areas of the coating, leaving residual holes within the coating [33]. In contrast, Si infiltration is a densification method that integrates physical filling and chemical reaction, and the strong diffusion capacity of Si has the ability to densify the entire coating [34,35]. Zhou et al. have successively prepared a series of Si-based ceramic coatings on the surface of C/C composites by slurry dipping combined with gaseous Si infiltration, such as SiC-Si [36], ZrB_2-SiC-Si/SiC-Si [37] and HfB_2-SiC-Si/SiC-Si [24] coatings, which demonstrated a great potential for the protection of C/C composites. The above studies indicate that the dense coatings obtained by slurry dipping combined with silicon infiltration are promising for oxidation protection of curved C/C composites at 1700 °C.

Up to date, there is little research carried out on the differences between gaseous and liquid Si infiltration processes for the oxidation protection of C/C composites in air at 1700 °C, especially for curved shaped components. It has been reported that microstructure and high-temperature properties of specimens are largely controlled by their shape characteristics and preparation processes [38–40]. Therefore, it is necessary to study the differences and mechanism of the densification effect of gaseous/liquid Si infiltration on curved pre-coated specimens and the oxidation resistance of the final coating, so as to provide a reference for the selection of the coating preparation process for curved shaped components.

In this work, a HfB_2-SiC-$MoSi_2$-Si/SiC-Si coating with a bilayer structure is prepared on C/C composites using pack cementation, slurry dipping combined with gaseous/liquid silicon infiltration. The evolution in composition and structure of the curved sample coatings on convex and concave regions by gaseous/liquid silicon infiltration are investigated. The isothermal oxidation and thermal shock behaviors at 1700 °C and protection mechanisms are discussed. This work provides guidance for manufacturing process selection of high-temperature oxidation-resistant coatings for carbon-based curved shaped components.

2. Experimental procedures

2.1. Material preparation

In experiment, 2.5D needle-punched carbon/carbon (C/C) composites with density of 1.7–1.8 g/cm^3 were processed into curved samples with a curvature radius of 7 mm. The fabrication process of HfB_2-SiC-$MoSi_2$/SiC coating is shown in Fig. 1. The SiC transition layer was prepared on curved C/C surfaces by pack cementation (PC) [41]. PC-SiC coated samples were dipped in a homogeneous slurry composed of phenolic resin (4–12 wt%, 99.9 % purity), absolute alcohol (40–60 wt%, AR), HfB_2 (0–30 wt%, 99.9 % purity), SiC (15–40 wt%, 99.9 % purity) and $MoSi_2$ (10–20 wt%, 99.9 % purity) to obtain the green coating. The green coated samples were cured at 150–300 °C for 1–4 h in an argon atmosphere and then carbonized at 900–1200 °C for 2–5 h to get HfB_2-SiC-$MoSi_2$ (HSM) pre-coating. Detailed slurry dipping and heat treatment processes were described in our previous work [42]. The porous pre-coating was densified by gaseous silicon infiltration (GSI) and liquid silicon infiltration (LSI), respectively. Details of GSI and LSI were as follows: (i) For GSI, the pre-coated samples were placed on a porous graphite plate in a graphite crucible. The bottom of the crucible was covered with silicon blocks. Then, the crucible was placed in an argon atmosphere at 1700–1900 °C for 0.5–2 h after sealing to obtain G-HSM coated curved C/C composites. (ii) For LSI, the pre-coated samples were buried in a powder mixture of Si (70–85 wt%, 40–50 μm, 99.0 % purity), graphite (10–25 wt%, 30–50 μm, 99.5 % purity) and SiC (5–15 wt%, 1–3 μm, 99.9 % purity). Then the crucible was heated to 1400–1600 °C with a holding time of 0.5–2 h to obtain L-HSM coated curved C/C composites.

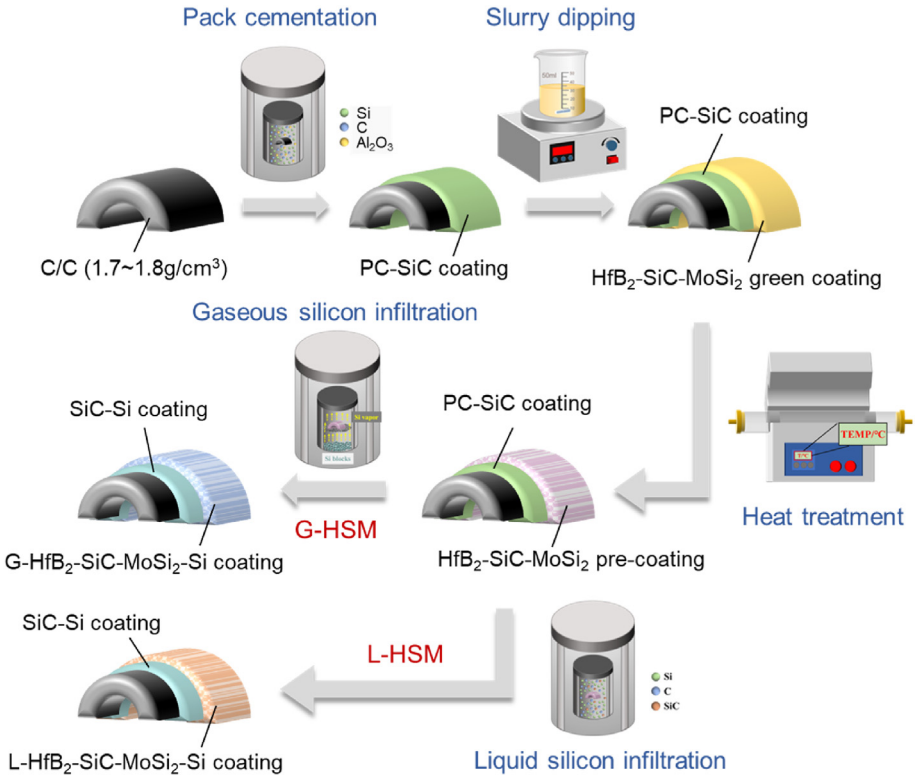

Fig. 1. Schematic diagram about the fabrication process of G-HSM and L-HSM.

2.2. Oxidation tests

The thermal cycling test between 1700 °C and room temperature and isothermal oxidation test at 1700 °C were used to evaluate the oxidation resistance of G-HSM and L-HSM. ZrO_2 pads was placed at the bottom of the alumina crucibles to hold the samples and prevent adhesion. Then putted the crucibles into the muffle furnace at 1700 °C. Samples were taken out at intervals and cooled to room temperature for weighing. Specifically, for the thermal cycling test, samples were kept at 1700 °C for 15 min and then removed and cooled at room temperature for 5 min. The mass change percentage was calculated according to

$$M = \frac{m_t - m_0}{m_0} \times 100\%, \quad (1)$$

where M is the mass change rate (%), m_0 is the mass of the samples before oxidation; m_t is the mass of the samples after oxidation.

2.3. Material characterization

Phase composition, microstructure and element distribution were characterized by X-ray diffractometer instrument (XRD, X'Pert Pro MPD) and scanning electron microscopy (SEM, Zeiss) equipped with an energy dispersive spectrometer (EDS, Oxford INCA), respectively. The average roughness (R_a) and three-dimensional (3D) profiles of G-HSM and L-HSM were determined by a non-contact profilometer (HS1000, Nanovea, USA). The content of Si + SiC and HfB_2 + $MoSi_2$ of the coating prepared by GSI and LSI was measured by Image J software.

The stress distribution of the coatings with GSI and LSI during preparation and thermal shock were carried out with Finite Element Analysis (FEA, ANSYS 19.0) method. The physical parameters of the materials used in the simulation models were presented in Table 1. Here ρ, E, ν, α, λ and C are the density, elastic modulus, Poisson's ratio, coefficient of thermal expansion, thermal conductivity and specific heat capacity, respectively.

3. Results and discussion

3.1. Microstructure and composition of coatings

Fig. 2 shows the phase composition of HSM pre-coating, G-HSM and L-HSM coating. The accumulation of white (HfB_2), gray ($MoSi_2$) and black (SiC) particles in the HSM pre-coating formed a porous structure, which facilitates subsequent silicon infiltration. Fig. 2b and c displays that the pre-coating thickness for both convex and concave areas is approximately 340 μm. G-HSM and L-HSM are both composed of white (HfB_2), light gray ($MoSi_2$), dark gray (Si) and black (SiC) phases as shown in Fig. 2d and g. SiC, HfB_2 and $MoSi_2$ in G-HSM are surrounded by a continuous Si to form a mosaic structure, the difference is that the four phases are interconnected to form a consecutive structure for L-HSM. To better clarify the phase content discrepancies of the two coatings, the volume fractions of Si + SiC and HfB_2 + $MoSi_2$ on the surface and cross-section of the coatings were calculated by Image J software. For the surface, the volume fractions of Si + SiC and HfB_2 + $MoSi_2$ in G-HSM and L-HSM are 86.8 %, 13.2 % and 90.7 %, 9.3 %, respectively. Correspondingly, for the cross-section, the volume fractions of Si + SiC and HfB_2 + $MoSi_2$ in G-HSM and L-HSM are 91.8 %, 8.2 % and 72.6 %, 27.4 %, respectively. In contrast, there are slightly less HfB_2 and $MoSi_2$ on the surface of L-HSM than G-HSM, and significantly more HfB_2 and $MoSi_2$ inside the coating than G-HSM. The pre-coating was combined by particle accumulation with low bonding strength, and the scour of uncontrollable silicon vapor on the outer coating at high temperature would drive the migration and falling off of the ultra-high temperature ceramic phases [25]. Such instability of GSI process will limit its application in curved parts. Instead, LSI eliminates the effects of gas scour and the UHTCs phases are retained within the coating, which may contribute to the high temperature stability of the coating in an aerobic environment.

Table 1
Parameters of the relevant materials in the FEA model.

Materials	ρ (kg/m^3)	E (GPa)	ν	α (10^{-6}K)	λ (W/m^2·K)	C (J/kg·K)
C/C [43]	1700	35	0.216	1.0	72	1800
$MoSi_2$ [43]	6240	408	0.166	7.8	45	471.5
HfB_2 [44]	11000	480	0.12	6.1	51	320
SiC [43]	3200	340	0.142	4.0	39	700

The thermal stress distributions of convex and concave regions during fabrication cooling were calculated for evaluation in Fig. 3a and c. The size parameters of the model were established in a ratio of 1:1 with the actual samples. The initial ambient temperature of GSI and LSI was set to 1700–1900 °C and 1400–1600 °C, respectively. The ambient cooling rate was defined as 5 °C/min. The thermal radiation heat transfer coefficient between samples and surrounding environment was 0.8 [45]. The thermal stress was evaluated based on a temperature change of 10 °C. The stress values in the convex and concave regions of G-HSM and L-HSM can be estimated to be 151.95 MPa, 134.63 MPa and 127.54 MPa, 113.21 MPa. The thermal stress of G-HSM is about 20 % higher than that of L-HSM, and the stress value in both convex area is higher than those in concave area. The surface crack size in different regions of G-HSM and L-HSM shown in Fig. 3d corresponds to the calculated thermal stress. Due to the relevantly higher preparation temperature of G-HSM, higher thermal stress was generated during the cooling process, which leads to more pronounced cracking. Affected by the impact of shape characteristics, the cracks in the convex region of both coatings were wider than those in the concave region.

Fig. 3e and f illustrate the cross-sectional morphologies of G-HSM and L-HSM. The porous structure formed by particle accumulation in the longitudinal direction of both coatings also disappeared, indicating the ability of both gaseous and liquid silicon to reach the targeted penetration depth. On account of the stronger scour of gaseous silicon on the concave region, some of the poorly bonded external porous pre-coatings fell off, so that the thickness of the G-HSM was significantly thinner than that of the pre-coating [46]. Compared to G-HSM, the coating thickness on the convex surface of the L-HSM was closer to the coating thickness on the concave surface. LSI avoids the negative effects of gas scour on porous pre-coatings and therefore maintains the original coating thickness and composition. From the cross-sectional images of the C/C substrate after GSI and LSI (Fig. 3g), the percentage area of siliconized region was 12.68 % and 5.12 % for G-HSM and L-HSM. Si vapor and melt enters the C/C through the open holes by gaseous diffusion and capillary force, respectively. The gaseous diffusion is stronger than the capillary force. The excessive penetration of Si tends to cause severe silicification damage, which is detrimental to the flexural properties of thin-walled C/C composites [47].

Fig. 3h gives the 3D profiles and average roughness (R_a) on a macroscopic scale for G-HSM and L-HSM coated samples. The result shows that the R_a values of the convex and concave surfaces of G-HSM and L-HSM are 11.60 μm, 14.50 μm and 5.73 μm, 5.16 μm, respectively. For G-HSM, the R_a of the concave surface is about 25 % higher than that of the convex surface, which is related to the more drastic erosion of the concave surface by high-temperature gaseous Si, while there is no significant difference in the R_a of the convex and concave surfaces L-HSM. Besides, the R_a of L-HSM is only within half of that of G-HSM, which is consistent with the microstructures shown in Fig. 2d and g. In general, the lager the surface roughness of the coating, the lager its surface area, and the more the oxygen adsorption sites [48,49] on the one hand, the larger thermal stress caused during rapid cooling process [50,51] on the other hand. Therefore, the increase in roughness is not favorable to the antioxidant performance.

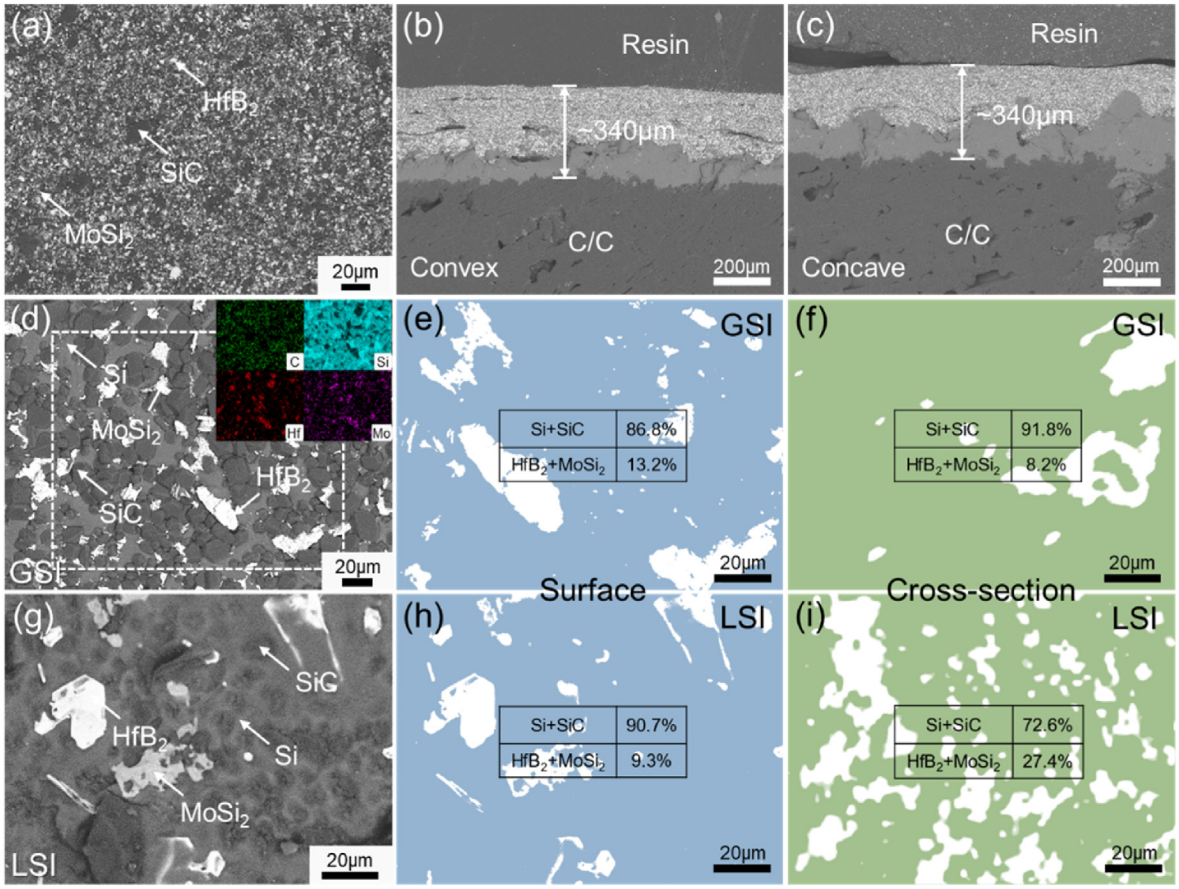

Fig. 2. Phase composition of HSM pre-coating, G-HSM and L-HSM coating. (a) Surface SEM image of HSM pre-coating, (b, c) cross-sectional SEM images of HSM pre-coating, (d, g) SEM images of local surface area, (e, h) phase content on the surface, (f, i) phase content in the cross-section.

3.2. Oxidation resistance of G-HSM and L-HSM at 1700 °C

The samples were subjected to a thermal cycling test from 1700 °C to room temperature. Fig. 4a shows the mass change and optical image of the samples after 20 thermal cycles. The optical image reveals that the surface of L-HSM is covered with a continuous bubble layer, and the coating remains intact without damage. The sample showed a mass gain of 0.07 % after 20 thermal cycles, demonstrating good thermal shock resistance performance. The volatilization of oxidation products at 1700 °C is the cause of the formation of bubbles on the sample surface. Compared to L-HSM, there were few bubbles on G-HSM surface, depending on the low content of HfB_2 and $MoSi_2$. With the increase of the number of thermal cycles, the mass of G-HSM is greatly lost. After 20 thermal cycles between 1700 °C and room temperature, the G-HSM coated sample lost 2.52 % of weight, which indicates the relatively poor thermal shock resistance of the coating. The mass changes of the above two curved samples during isothermal oxidation at 1700 °C are shown in Fig. 4b. The mass decay of G-HSM after 124 h of oxidation was 0.60 %, while the mass decay of L-HSM after 200 h of oxidation was only 0.12 %. According to the oxidation resistance of the coatings at 1700 °C reported by other works [17,20,29,33,52–56], L-HSM coating in this study exhibits excellent oxidation protection performance as shown in Fig. 4c.

According to the isothermal oxidation curves (Fig. 4b), the oxidation process was divided into three stages with the standard of G-HSM, which were marked as I, II and III. The mass loss curve of G-HSM exhibited a parabolic pattern. By contrast, the mass of L-HSM was relatively stable throughout the oxidation process. In the initial stage of oxidation (I), both samples presented a trend of weight increase. The mass of G-HSM rapidly increased by 3.25 % within the first 22 h. This is because HfB_2 and $MoSi_2$ were mainly distributed on the surface of the coating after GSI (Fig. 2). The generation of HfO_2, B_2O_3 and SiO_2 led to a quick weight gain in sample. At the same time, L-HSM had a mass gain of 0.32 % in stage I. During stage II, G-HSM continued to gain weight with a decrease in the rate of mass gain. After 92 h of oxidation, the mass increased by 4.63 %. The decrease in mass gain rate was related to the reduction of HfB_2 and $MoSi_2$, as well as the volatilization of gas products. For L-HSM, the mass loss due to volatilization of gaseous products and the mass gain from the oxidation of HfB_2, $MoSi_2$ and SiC reached equilibrium as the oxidation time increased [24]. Accordingly, the mass of L-HSM did not change significantly during this stage. In stage III, the mass of G-HSM deteriorated sharply, which manifested that coating failure led to the oxidation of C/C substrate. In this stage, the low-speed weight reduction of L-HSM indicated that the coating still held excellent oxygen resistance performance within 200 h.

In order to better elucidate the surface state of G-HSM and L-HSM after long-term isothermal oxidation, the 3D profiles and surface roughness of the two coated samples were evaluated (Fig. 4d). The surface of G-HSM became rough and uneven after oxidation for 124 h. The formation of bumps and pits on the surface illustrated that the coating had broken down. Quantitatively speaking, the roughness of the convex and concave areas reached 29.65 μm and 47.21 μm, respectively. R_a showed a pattern that the roughness of the concave surface was generally lager than that of the convex surface, which corresponded to the unoxidized coating samples. An area of 3×9 mm^2 was selected at the center of the convex and concave surfaces of the sample to further evaluate the surface condition. The local areas of sudden color changes represented macro-defects of the coating surface. Compared to G-HSM, the continuous color change of L-HSM symbolized a lesser undulating surface after 200 h of oxidation, and no obvious deep bumps and pits were found. The roughness of the convex and concave surfaces of the L-HSM was similar

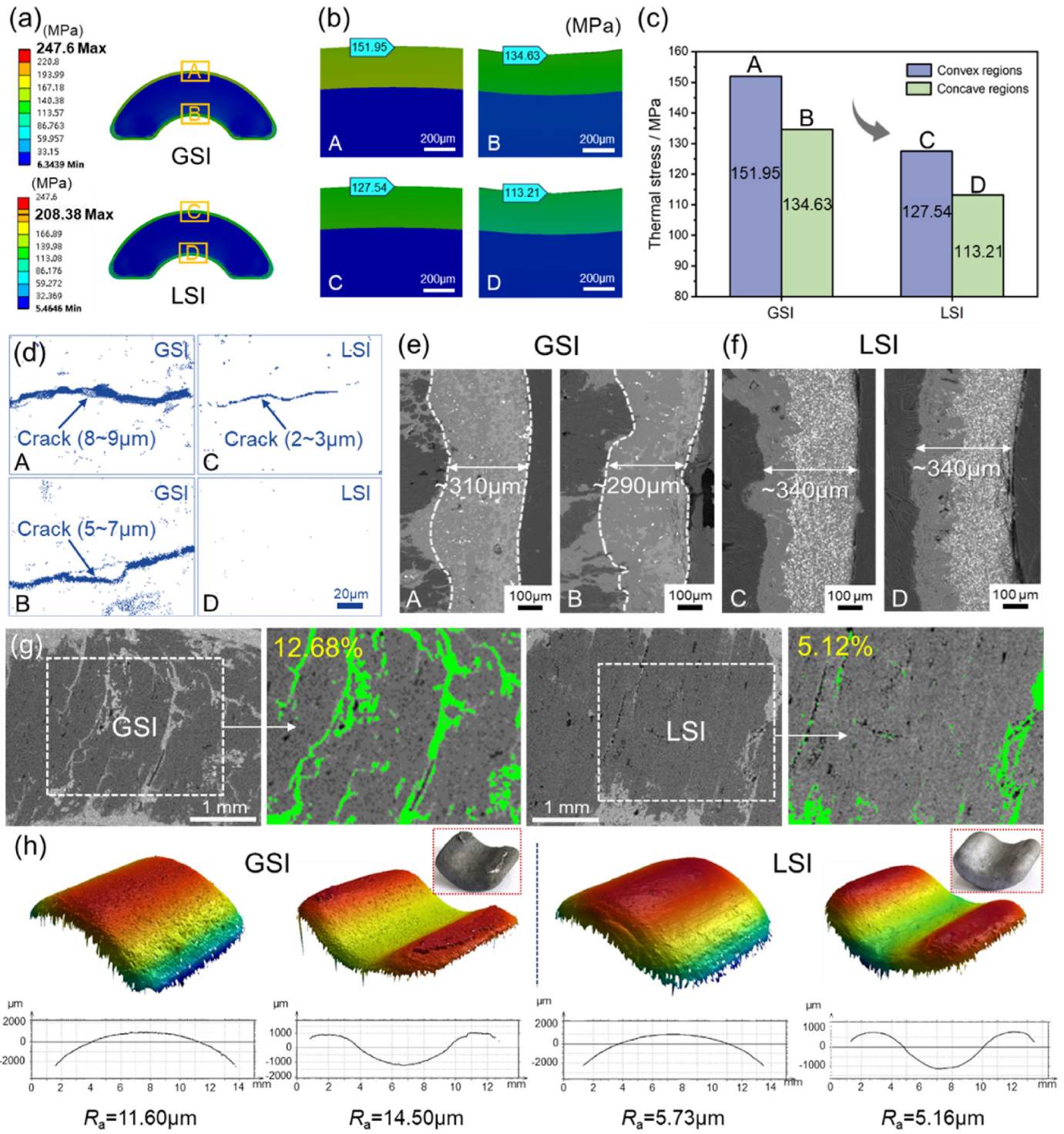

Fig. 3. Micro/macro morphology differences of G-HSM and L-HSM. (a–c) The thermal stress distribution during coating fabrication cooling, (d) surface crack condition, (e, f) coating cross-sectional morphologies, (g) C/C substrate cross-sectional morphologies, (h) macroscopic three-dimensional contours.

in magnitude ($R_a = 17.36$ μm in the convex region, $R_a = 18.14$ μm in the concave region) and decreased significantly with respect to the G-HSM. The above findings suggest that the L-HSM coating still remained intact after long-term isothermal oxidation.

Fig. 5a shows similar results for XRD patterns of G-HSM and L-HSM after thermal cycling. The main diffraction peaks correspond to SiO_2, HfO_2 and a small amount of $HfSiO_4$ and SiC. The oxides are generated by Eqs. (2)–(6) [57,58]. Unlike thermal cycling, the peak intensity of high-temperature stable phase $HfSiO_4$ of L-HSM increases after isothermal oxidation from Fig. 5b. This is because the HfO_2 and SiO_2 produced by the original coating components during long-duration oxidation fully react (Eq. (6)). By comparison, the principal phase of G-HSM remains SiO_2, which is related to the fact that HfO_2 in G-HSM was not sufficient to generate large amount of $HfSiO_4$ during the long-duration oxidation.

$$Si\ (l) + O_2\ (g) = SiO_2\ (l), \tag{2}$$

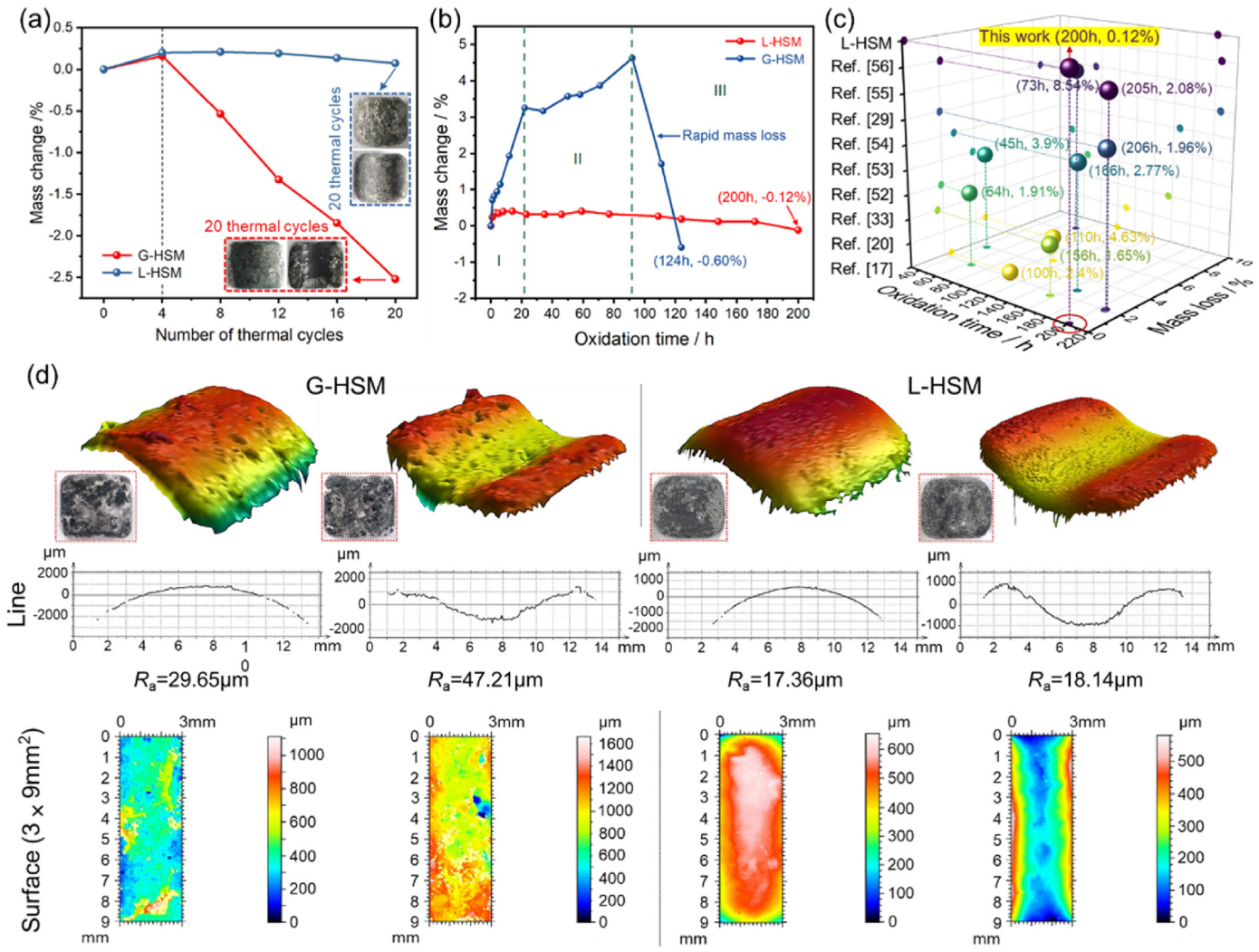

Fig. 4. Oxidation resistance of G-HSM and L-HSM. (a) Mass change curves during thermal cycling between 1700 °C and temperature, (b) mass change curves during isothermal oxidation at 1700 °C, (c) comparison of oxidation resistance between this work and other works at 1700 °C [17,20,29,33,52–56], (d) three-dimensional contours after oxidation.

$$2\ Si\ (l) + O_2\ (g) = 2\ SiO\ (g), \quad (3)$$

$$1/2\ SiC\ (s) + O_2\ (g) = 1/2\ SiO_2\ (l) + 1/2\ CO_2\ (g), \quad (4)$$

$$2/5\ HfB_2\ (s) + O_2\ (g) = 2/5\ HfO_2\ (s) + 2/5\ B_2O_3\ (l), \quad (5)$$

$$HfO_2\ (s) + SiO_2\ (l) = HfSiO_4\ (s). \quad (6)$$

Fig. 5c presents the Gibbs free energy curves of active oxidation of Si and SiC. It is found that active oxidation intensifies with increasing temperature, which might lead to the escape of more gas products. Fig. 5d shows the saturated vapor pressure at different temperatures of SiO_2, Si, B_2O_3, HfO_2 and MoO_3. Based on the physical properties of the material, the vapor pressure of 10^{-2}-10^{1} Pa is the critical value for the stability of the material in the gas phase [59]. At a critical value of 10^{-2} Pa, 1700 °C exceeds the critical tolerance temperature of SiO_2, Si, B_2O_3, and MoO_3, causing them to transform into gas phase. The active oxidation of Si and SiC and the volatilization of SiO_2, Si, B_2O_3 and MoO_3 might result in a large number of gaseous products escaping from the surface of the sample to form holes and bubbles. The critical tolerance temperature of SiO_2 is 1677 °C, which shows a relatively low loss rate. Notably, HfO_2 and $HfSiO_4$ remained stable at 1700 °C and helped to further inhibit the volatilization of SiO_2 [60], which facilitated the enhanced oxidation protective ability of this coating at 1700 °C.

3.3. Oxidation behavior and mechanism of G-HSM and L-HSM at 1700 °C

To further clarify the evolution of the coating microstructure after oxidation, surface and cross-sectional SEM images of the oxidized coating were presented. It is found that various regions of the two curved samples exhibited different morphological characteristics. Fig. 6 shows the microcosmic morphologies of G-HSM and L-HSM after 20 thermal cycles. Holes and cracks appeared on the surface of G-HSM due to the volatilization of gas products and the sudden temperature changes during thermal shock (Fig. 6a). Notably, Hf was carried by the low-viscosity phase (SiO_2) that melts at high temperature, forming large droplets with a diameter of about 600 μm at the edge of the concave region of the sample (Fig. 6b and c). For L-HSM, bubbles were evenly distributed on the surface of the coating (Fig. 6d and e), corresponding to the macroscopic optical image of L-HSM (Fig. 4a). White phase aggregation was observed on the surface of SiO_2 bubbles, which was confirmed by EDS to be HfO_2/$HfSiO_4$ compounds. Compared to G-HSM, the L-HSM surface was covered with a large number of bubbles. On the one hand, it is due to the relatively high content of HfB_2 and $MoSi_2$, thus more gaseous oxidation products B_2O_3 and MoO_3 were generated during oxidation processes, on the other hand, HfO_2/$HfSiO_4$ phases contribute to inhibit the volatilization of SiO_2 [37], thus allowing the surface SiO_2 to remain

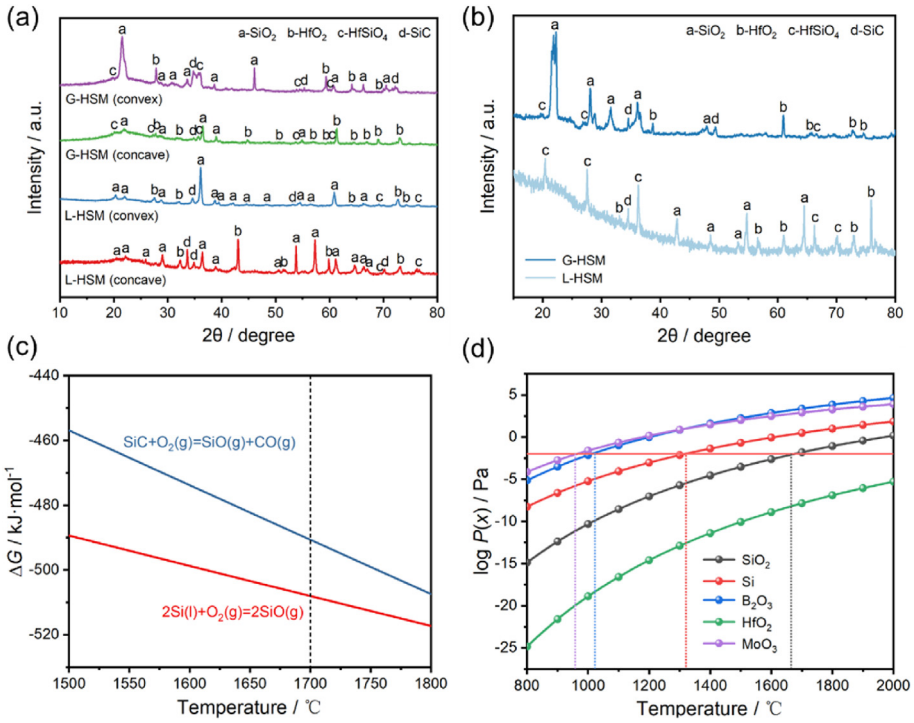

Fig. 5. XRD patterns after oxidation, Gibbs free energy of oxidation reactions and saturated vapor pressure of oxidation products. (a) XRD patterns of G-HSM and L-HSM after thermal cycling test, (b) XRD patterns of G-HSM and L-HSM after isothermal oxidation test, (c) Gibbs free energy curves, (d) saturated vapor pressure at different temperatures.

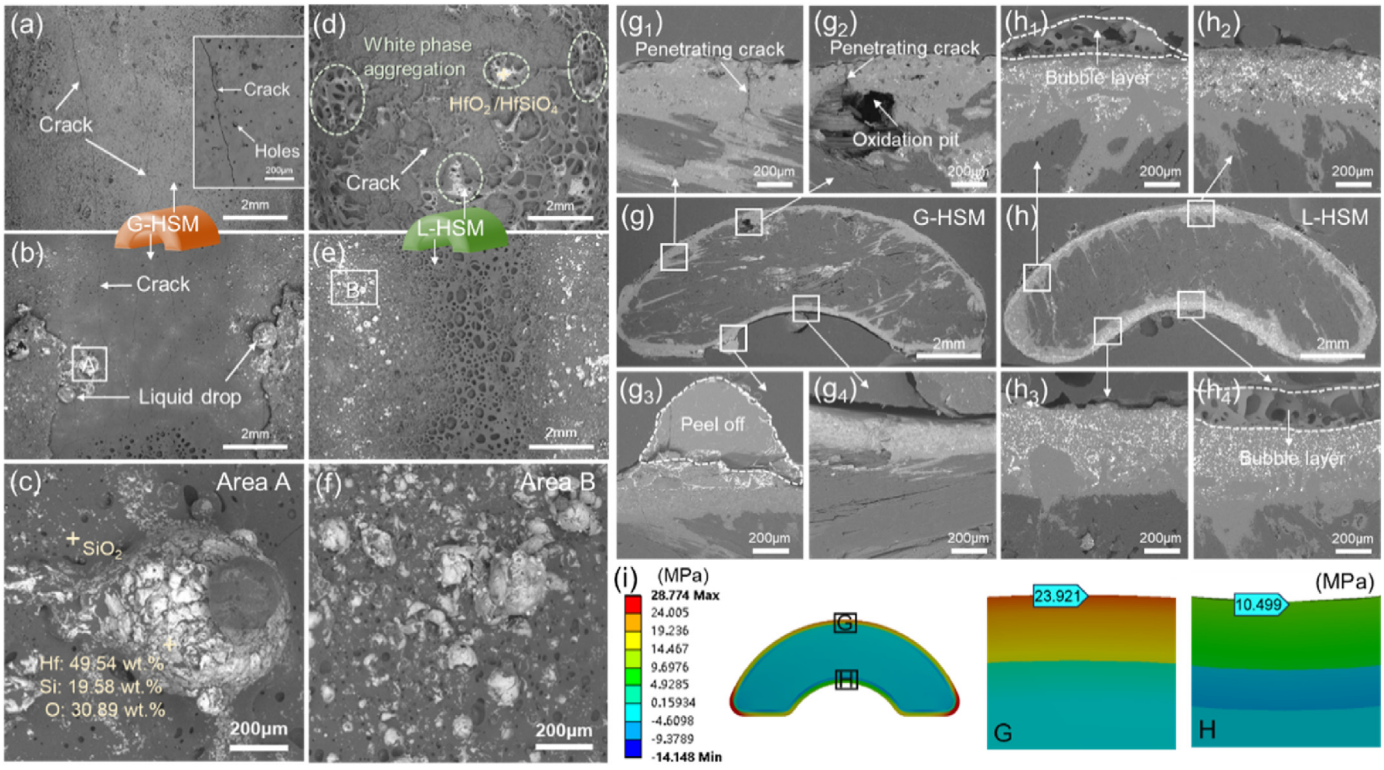

Fig. 6. Microcosmic morphologies and thermal stress distribution after thermal cycling. (a–c) surface SEM images of G-HSM, (d–f) surface SEM images of L-HSM, (g_1-g_4) cross-sectional SEM images of G-HSM, (h_1-h_4) cross-sectional SEM images of L-HSM, (i) thermal stress distribution during a thermal cycle between 1700 °C and room temperature.

in the form of bubbles, while reducing mass loss. In addition, the droplet size at the concave edge of the L-HSM was significantly reduced compared to the G-HSM, reducing the risk of droplet falling (Fig. 6f).

The cross sections of G-HSM and L-HSM after 20 thermal cycles are shown in Fig. 6g and h. It can be observed that penetrating cracks were present in the convex region of G-HSM (Fig. 6g_1 and g_2). The appearance of oxidation pit at the cracked end indicates coating failure, corresponding to the rapid mass loss of the thermal cycling curve in Fig. 4a. By comparison, no obvious penetrating cracks were found in the concave region (Fig. 6g_3 and g_4), which might be related to the stress caused by thermal shock at the process of temperature change [61,62]. The flaking of the coating at the concave edge was consistent with the sliding of liquid droplets on the surface in Fig. 6c. The massive shedding of droplets from the coating surface also contributes to the mass loss of G-HSM. In contrast, after 20 thermal cycles, L-HSM remained dense and the ultra-high temperature phases were uniformly distributed in the coating as shown in Fig. 7h_1-h_4. There were no obvious oxidation defects in C/C substrate, which implies that L-HSM has excellent thermal shock resistance. In order to further illustrate the discrepancy of oxidation degree in different regions of G-HSM and clarify the failure mechanism, thermal stress distribution during a thermal cycle from 1700 °C to room temperature was simulated by FEA as shown in Fig. 6i. The result reveals that the thermal stress in the convex region of the curved sample is 23.92 MPa, which is 127.8 % higher than that in the concave region (10.50 MPa). From the fracture mechanics theory, it is known that once the residual stress exceeds the damage tolerance of the material, the cracks existing in the structure will expand into critical cracks [63]. To put it in another way, the microcracks within the coating induced by excessive residual stress in the convex region increased with the number of thermal shocks, and the microcracks gradually developed to form penetrating cracks [45]. As a result, penetrating cracks were more likely to form in the convex region of G-HSM, providing a channel for oxygen diffusion into the interior of the C/C substrate. For L-HSM, the high-temperature stabilized phases contribute to inhibit crack propagation, thus reducing the probability of penetrating crack formation.

Fig. 7 illustrates the surface and cross-sectional morphologies of G-HSM and L-HSM after long-duration isothermal oxidation at 1700 °C. From the surface images (Fig. 7a), G-HSM is composed of a black SiO_2 framework with a small number of white particles dispersed on the surface. It presents a rough surface state after long-term isothermal oxidation, which corresponds to Fig. 4d. There are numerous holes on the SiO_2 framework, which is more pronounced than those of holes during thermal shock. This is related to the more gas products produced by prolonged oxidation. Further observation reveals the presence of cracks, which is caused by multiple thermal shocks from 1700 °C to room temperature during the oxidation test process [64]. The local coating peeling and oxidative corrosion pits in the concave area of the sample were observed from the macroscopic cross-section of G-HSM in Fig. 7b. The oxidation of C/C substrate is the reason for rapid mass loss of stage III. The local cross-sectional view of G-HSM shows penetrating cracks and oxidation pits left by the oxidation of the substrate (Fig. 7c). In addition, the thickness of the coating decreased after oxidation, which is due to the significant loss of SiO_2-rich oxide scale at 1700 °C [36]. From the macroscopic cross-section of L-HSM, it can be observed that the sample is wrapped in a bubble oxide layer (Fig. 7e). For L-HSM, the C/C substrate is not oxidized and the volume expansion of the oxide scale slightly increases the coating thickness of L-HSM. Corresponding to the macroscopic optical images, there are also many bubbles on the microscopic surface of the coating (Fig. 7d–f). Furthermore, it is observed that a large number of white phases are embedded on the gray SiO_2 skeleton. Previous studies have shown that the white pinning phases can inhibit the volatilization of SiO_2 [37,65], which contributes to integrity of the internal coating and confirms the phenomenon of no thinning of the coating. The oxide scale of L-HSM was thinner than that of G-HSM from the distribution of oxygen in the cross-section, which illustrates that L-HSM has better oxygen isolation capacity on curved samples.

The oxidation mechanism of G-HSM and L-HSM is concluded in Fig. 7g and illustrated as follows.

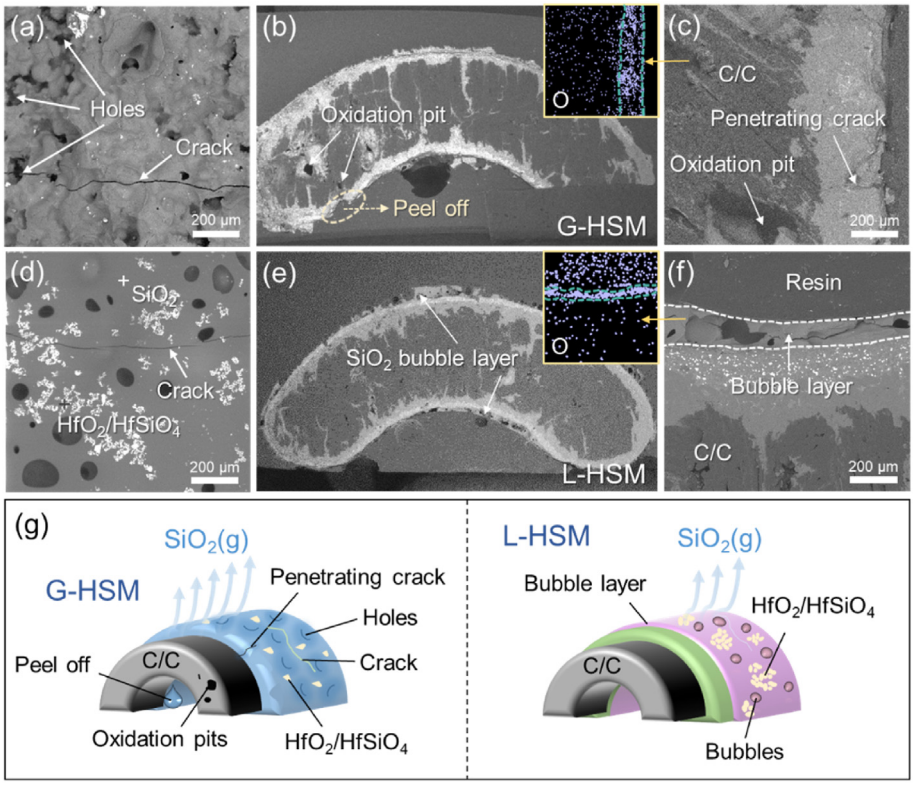

Fig. 7. Microcosmic morphologies of G-HSM and L-HSM after isothermal oxidation and the oxidation mechanism. (a–c) SEM images of G-HSM, (d–f) SEM images of L-HSM, (g) oxidation mechanism diagram.

(i) For G-HSM, due to the high content of Si and SiC, their active oxidation at 1700 °C would cause extensive gas volatilization [66]. At the same time, the lack of HfO_2/$HfSiO_4$ compounds that could inhibit the volatilization of SiO_2 and prevent the crack propagation would produce a large number of holes and cracks on the surface of the coating. In addition, the main phase of the coating after oxidation was low viscosity SiO_2, which increased the fluidity of the coating. Affected by gravity and the inherent slope feature of curved samples [42], The SiO_2 melting at 1700 °C carried Hf and Mo to form large-sized droplets that gradually slipped to the edge of the sample and fell off after a long period of oxidation. The loss of local coating not only induced mass decay, but also caused local stress concentration [67] and led to the initiation of penetrating cracks, which would give rise to severe oxidation of the C/C substrate.

(ii) For L-HSM, SiO_2 generated by the oxidation of sufficient $MoSi_2$ could heal defects in time [68]. HfO_2/$HfSiO_4$ pinning phases contributed to inhibit the volatilization of SiO_2, thus forming a continuous SiO_2-rich bubble layer on the coating surface. Such a structure enclosed by a bubble-rich oxide scale could effectively mitigate the oxidation inside the coating. Furthermore, the doping of HfB_2 and $MoSi_2$ helps to improve the viscosity of oxidation scale [44,69], which is the reason why no obvious droplet shedding was observed in the edge region and the coating remained intact.

4. Conclusions

In this work, porous HfB_2-SiC-$MoSi_2$ pre-coating has been densified with gaseous and liquid silicon for curved samples. The effects of different densification processes on curved samples are explored by comparing the macro/micro-structure and oxidation resistance of G-HSM and L-HSM at 1700 °C. Compared to G-HSM, L-HSM shows the more excellent thermal shock and long-duration isothermal oxidation resistance. The mass loss of G-HSM and L-HSM after 20 thermal cycles are 2.52 % and −0.07 %, respectively. The mass loss of G-HSM oxidized for 124 h and L-HSM oxidized for 200 h are 0.60 % and 0.12 %, respectively. The negative mass decay after thermal cycling and the near-zero mass loss percentage after isothermal oxidation of L-HSM provide insights for the coating design of special-shaped components above 1700 °C. The excellent oxidation resistance of L-HSM relative to G-HSM is attributed to the smaller thermal stress and crack size, the integrity and lower roughness of the coating after LSI. In addition, sufficient HfB_2 and $MoSi_2$ not only help to inhibit the volatilization of the oxide scale, but also improve the viscosity of the coating, thus effectively avoiding droplet shedding caused by gravity factors and the slope characteristics of curved samples, which is crucial to improve the performance of carbon-based special-shaped components to withstand aerobic environments above 1700 °C.

CRediT authorship contribution statement

Shubo Zhang: Writing – original draft, Methodology, Formal analysis, Data curation. **Zhiqiang Liu:** Writing – review & editing, Methodology, Formal analysis. **Shuo Zhang:** Methodology. **Xiaoxuan Su:** Writing – review & editing. **Qiangang Fu:** Writing – review & editing, Funding acquisition, Conceptualization.

Data availability

The raw/processed data needed to reproduce these findings cannot be shared at this time for technical and time limitations.

Declaration of competing interest

The authors declare that they have no known competing financial interests or personal relationships that could have appeared to influence the work reported in this paper.

Acknowledgements

This work has been supported by the National Key Research and Development Program of China (2021YFA0715800), the Science Center for Gas Turbine Project (P2021-A-IV-003-001), and the National Natural Science Foundation of China (52125203, 52432003).

References

[1] H. Qi, R. Ma, G. Meng, M. Liu, G. Yang, Research progress on aluminized coatings for high temperature blades, Cailiao Baohu 55 (2022) 147–161, https://doi.org/10.16577/j.issn.1001-1560.2022.0291.
[2] S. Yang, S. Gao, W. Xue, B. Wu, D. Duan, Oxidation and hot corrosion behaviors of NiAlTa protective material for turbine single crystal blade tips, Corros. Sci. 230 (2024) 111899, https://doi.org/10.1016/j.corsci.2024.111899.
[3] Z. Zhao, K. Li, G. Kou, W. Li, Comparative research on cyclic ablation behavior of C/C-ZrC-SiC and C/C-ZrC composites at temperatures above 2000 °C, Corros. Sci. 206 (2022) 110496, https://doi.org/10.1016/j.corsci.2022.110496.
[4] W. Guo, S. Bai, Y. Ye, Controllable fabrication and mechanical properties of C/C-SiC composites based on an electromagnetic induction heating reactive melt infiltration, J. Eur. Ceram. Soc. 41 (2021) 2347–2355, https://doi.org/10.1016/j.jeurceramsoc.2020.11.018.
[5] Y. Peng, Z. Li, A. Li, Q. Wang, R. Bai, F. Zhang, Mechanical and tribological properties of C/C-SiC ceramic composites with different preforms, Sci. Eng. Compos. Mater. 30 (2023) 20220205, https://doi.org/10.1515/secm-2022-0205.
[6] J. Xu, L. Guo, J. Kong, Y. Ma, H. Wang, J. Wang, The mechanical properties of C/C-ZrC-SiC composites after laser ablation, J. Eur. Ceram. Soc. 43 (2023) 6732–6745, https://doi.org/10.1016/j.jeurceramsoc.2023.07.045.
[7] X. Shen, N. Gao, Z. Shi, X. Wang, L. Zhang, J. Huang, K. Li, New insight into the ablation behavior of C/C-ZrC composites in a nitrogen plasma torch with a high heat flux of ~25 MW/m^2, Corros. Sci. 185 (2021) 109409, https://doi.org/10.1016/j.corsci.2021.109409.
[8] J. Wang, L. Xu, W. Li, Y. Song, Z. Fan, Y. Liu, X. Li, T. Li, Z. Xu, Z. Feng, Research progress on C/C composites for aerospace applications, Aerospace. Mater. Technol. 52 (2022) 1–12 (in Chinese).
[9] Z.Q. Liu, Q.A. Fu, H.L. Shi, J.P. Zhang, Y.J. Jia, Comparative study of microstructure and ablation behaviour of C/C-HfC-SiC composites prepared under two different conditions, Mater. Char. 194 (2022) 112467, https://doi.org/10.1016/j.matchar.2022.112467.
[10] T. Li, Y. Zhang, J. Li, J. Lv, K. Shuai, Improved mechanical strength and oxidation resistance of SiC/SiC-$MoSi_2$-ZrB_2 coated C/C composites by a novel strategy, Corros. Sci. 205 (2022) 110419, https://doi.org/10.1016/j.corsci.2022.110419.
[11] X. Xie, X. Tang, Z.A. Su, J. Liao, C. Yang, Q. Huang, Oxidation and ablation behaviours of a SiCnw@SiC-Si coating fabricated for carbon-fibre-reinforced carbon-matrix composites via thermal evaporation and gaseous silicon infiltration, Ceram. Int. 49 (2023) 9130–9137, https://doi.org/10.1016/j.ceramint.2022.11.072.
[12] Z. Wen, C. Hou, M. Zhao, X. Wan, A peridynamic model for coupled thermo-mechanical-oxygenic analysis of C/C composites with SiC coating, Compos. Struct. 323 (2023) 117441, https://doi.org/10.1016/j.compstruct.2023.117441.
[13] J. Li, M. Hu, X. Qiu, B. Zhang, Y. Peng, S. Chen, Study on oxidation resistant coatings for ZrC modified C/C composites, China Ceram 59 (2023) 39–47 (in Chinese).
[14] Y. Xu, W. Sun, C. Miao, Y. Shen, H. Chen, Y. Liu, H. Zhang, X. Xiong, Ablation properties of C/C-UHTCs and their preparation by reactive infiltration of K_2MeF_6 (Me = Zr, Ti) molten salt, J. Eur. Ceram. Soc. 41 (2021) 5405–5416, https://doi.org/10.1016/j.jeurceramsoc.2021.04.043.
[15] S. Kou, Y. Mao, J. Ma, Y. Ma, S. Yang, X. Liu, S. Fan, C. Liu, Microstructure evolution and properties of Hf/Zr-based UHTCs modified C/C composites prepared by reactive melt infiltration method, J. Eur. Ceram. Soc. 44 (2024) 3610–3621, https://doi.org/10.1016/j.jeurceramsoc.2023.12.078.
[16] Z. Liu, Y. Jia, J. Hou, R. Zhang, S. Zhang, J. Zhang, Q. Fu, C/C-HfC-SiC composites with simultaneous the resistance to ultra-high temperature airflow erosion and high temperature oxidation, J. Materiomics 11 (2025) 100846, https://doi.org/10.1016/j.jmat.2024.02.006.
[17] L. Zhou, J. Zhang, D. Hu, Q. Fu, W. Ding, J. Hou, B. Liu, M. Tong, High temperature oxidation and ablation behaviors of HfB_2-SiC/SiC coatings for carbon/carbon composites fabricated by dipping-carbonization assisted pack cementation, J. Mater. Sci. Technol. 111 (2022) 88–98, https://doi.org/10.1016/j.jmst.2021.08.092.
[18] X. Zhu, Y. Zhang, J. Zhang, Y. Su, R. Chen, P. Zhang, SiC/HfB_2-based ceramic/SiC multilayer coating to protect C/C composites against oxidation at medium and high temperatures for long-life service, Corros. Sci. 201 (2022) 110299, https://doi.org/10.1016/j.corsci.2022.110299.
[19] K. Li, G. Liu, Y. Zhang, Ablation properties of HfB_2 coatings prepared by supersonic atmospheric plasma spraying for SiC-coated carbon/carbon composites, Surf. Coat. Technol. 357 (2019) 48–56, https://doi.org/10.1016/j.surfcoat.2018.09.060.
[20] X. Zhu, C. Ou, T. Li, Y. Zhang, J. Lv, R. Chen, $HfSi_2$-HfB_2-SiC coating prepared at low temperature to protect SiC-coated C/C composites against oxidation at 1473-1973 K, Ceram. Int. 50 (2024) 13490–13499, https://doi.org/10.1016/j.ceramint.2024.01.261.

[21] P. Lespade, N. Richet, P. Goursat, Oxidation resistance of HfB_2-SiC composites for protection of carbon-based materials, Acta Astronaut. 60 (2007) 858–864, https://doi.org/10.1016/j.actaastro.2006.11.007.

[22] A.Y. Potanin, A.N. Astapov, Y.S. Pogozhev, S.I. Rupasov, N.V. Shvyndina, V.V. Klechkovskaya, E.A. Levashov, I.A. Timofeev, A.N. Timofeev, Oxidation of HfB_2-SiC ceramics under static and dynamic conditions, J. Eur. Ceram. Soc. 41 (2021) 34–47, https://doi.org/10.1016/j.jeurceramsoc.2021.09.018.

[23] P. Wang, H. Li, J. Sun, R. Yuan, L. Zhang, Y. Zhang, T. Li, The effect of HfB_2 content on the oxidation and thermal shock resistance of SiC coating, Surf. Coat. Technol. 339 (2018) 124–131, https://doi.org/10.1016/j.surfcoat.2018.02.029.

[24] L. Zhou, J. Zhang, D. Hu, Q. Fu, J. Zhu, J. Song, W. Ding, J. Hou, M. Tong, Investigation on the oxidation and ablation behaviors of HfB_2-SiC-Si/SiC-Si coatings for carbon/carbon composites, Corros. Sci. 190 (2021) 109638, https://doi.org/10.1016/j.corsci.2021.109638.

[25] Y. Wang, L. Guo, Y. Zhang, X. Zhang, H. Ou, J. Sun, Ablation behaviors and mechanism of ZrC-SiC-Si/SiC-Si double-layered coatings on C/C composite under plasma flame at 3000 °C, Corros. Sci. 218 (2023) 111200, https://doi.org/10.1016/j.corsci.2023.111200.

[26] L. Silvestroni, G. Meriggi, D. Sciti, Oxidation behavior of ZrB_2 composites doped with various transition metal silicides, Corros. Sci. 83 (2014) 281–291, https://doi.org/10.1016/j.corsci.2014.02.026.

[27] L. Wang, Q.G. Fu, N.K. Liu, Y.C. Shan, Supersonic plasma sprayed $MoSi_2$-ZrB_2 antioxidation coating for SiC-C/C composites, Surf, Eng 32 (2016) 508–513, https://doi.org/10.1179/1743294415Y.0000000098.

[28] W. Ding, L. Zhou, J. Zhang, Q. Fu, Long-term oxidation of $MoSi_2$-modified HfB_2-SiC-Si/SiC-Si coating at 1700 °C, Surf, Eng. 39 (2023) 315–325, https://doi.org/10.1080/02670844.2023.2223454.

[29] T. Li, Y. Zhang, J. Lv, Y. Fu, J. Sun, X. Qiang, A novel $MoSi_2$-rich coating on the SiC-Si coated C/C composites for the preparation and antioxidative properties at 1773 K and 1973 K, Corros. Sci. 204 (2022) 110392, https://doi.org/10.1016/j.corsci.2022.110392.

[30] T. Li, Y. Zhang, J. Lv, Y. Fu, J. Zhang, Eliminated siliconization corrosion and improved oxidation resistances of SiC-Si coated C/C composites via a ZrB_2-rich transition layer, Corros. Sci. 195 (2022) 109986, https://doi.org/10.1016/j.corsci.2021.109986.

[31] Z. Tang, M. Yi, H. Wu, Y. Zhou, R. Liu, J. Jiang, K. Peng, A novel approach for preparing a SiC coating on a C/C-SiC composite by slurry painting and chemical vapor reaction, J. Eur. Ceram. Soc. 42 (2022) 1884–1892, https://doi.org/10.1016/j.jeurceramsoc.2022.01.022.

[32] M.M. Shao, Z.K. Chen, X.S. Wang, Q.B. Wen, X. Xiong, Ablation behavior and mechanisms of ZrC-SiC-$MoSi_2$ coated C/C-SiC-ZrC ceramic matrix composites under oxyacetylene torch, Trans. Nonferrous Metals Soc. China 33 (2023) 220–230, https://doi.org/10.1016/S1003-6326(22)66102-8.

[33] J. Lv, Y. Zhang, W. Li, X. Zhu, J. Li, J. Zhang, T. Li, Microstructure evolution of HfB_2-SiC/SiC coating for C/C composites during long-term oxidation at 1700 °C, Corros. Sci. 206 (2022) 110524, https://doi.org/10.1016/j.corsci.2022.110524.

[34] Z. Liu, W. Zhang, H. Bu, K. Chen, Y. Jiang, H. Liu, C. Zeng, Antioxidant performance and oxidation mechanism of a liquid silicon infiltration (LSI) SiC-Si coating at an ultra-high temperature of 1873 K, Ceram. Int. 49 (2023) 34038–34052, https://doi.org/10.1016/j.ceramint.2023.08.104.

[35] P. Tang, C. Hu, Y. Jiang, M. Yan, S. Pang, R. Zhao, L. Wang, S. Tang, Facile preparation of SiC/ZrB_2-SiC-Si coatings on Cf/SiC composites for ultrahigh temperature ablation resistance, Corros. Sci. 232 (2024) 112051, https://doi.org/10.1016/j.corsci.2024.112051.

[36] L. Zhou, Q. Fu, D. Hu, Y. Wei, M. Tong, J. Zhang, Oxidation protective SiC-Si coating for carbon/carbon composites by gaseous silicon infiltration and pack cementation: a comparative investigation, J. Eur. Ceram. Soc. 41 (2021) 194–203, https://doi.org/10.1016/j.jeurceramsoc.2020.07.040.

[37] L. Zhou, Q. Fu, D. Hu, J. Zhang, Y. Wei, J. Zhu, J. Song, M. Tong, A dense ZrB_2-SiC-Si/SiC-Si coating to protect carbon/carbon composites against oxidation at 1773 K and 1973 K, Corros. Sci. 183 (2021) 109331, https://doi.org/10.1016/j.corsci.2021.109331.

[38] D. Sciti, A. Vinci, L. Zoli, P. Galizia, S. Failla, S. Mungiguerra, G.D. Di Martino, A. Cecere, R. Savino, Propulsion tests on ultra-high-temperature ceramic matrix composites for reusable rocket nozzles, J. Adv. Ceram. 12 (2023) 1345–1360, https://doi.org/10.26599/JAC.2023.9220759.

[39] R. Wang, N. Li, J. Zhang, B. Liu, N. Yan, Q. Fu, Ablation behavior of sharp leading-edge C/C-ZrC-SiC composites using 3000 °C oxyacetylene torch, Corros. Sci. 206 (2022) 110551, https://doi.org/10.1016/j.corsci.2022.110551.

[40] F. Monteverde, R. Savino, M.D.S. Fumo, A. Di Maso, Plasma wind tunnel testing of ultra-high temperature ZrB_2-SiC composites under hypersonic re-entry conditions, J. Eur. Ceram. Soc. 30 (2010) 2313–2321, https://doi.org/10.1016/j.jeurceramsoc.2010.01.029.

[41] T. Li, Y. Zhang, Y. Fu, J. Sun, J. Li, Siliconization elimination for SiC coated C/C composites by a pyrolytic carbon coating and the consequent improvement of the mechanical property and oxidation resistances, J. Eur. Ceram. Soc. 41 (2021) 5046–5055, https://doi.org/10.1016/j.jeurceramsoc.2021.04.008.

[42] S. Zhang, Q. Fu, Z. Dong, Z. Liu, H. Ou, X. Su, Effect of curvature radius on the oxidation protective ability of HfB_2-SiC-$MoSi_2$-Si/SiC-Si coating for C/C composites, Surf. Coat. Technol. 489 (2024) 131125, https://doi.org/10.1016/j.surfcoat.2024.131125.

[43] D. Hu, Q. Fu, L. Zhou, Y. Zhang, G. Zhang, Stress design of a laminated $MoSi_2$/Cr coating under particle impact and high temperature environment, Ceram. Int. 46 (2020) 10696–10703, https://doi.org/10.1016/j.ceramint.2020.01.076.

[44] J. Zhang, J. Hou, R. Wang, R. Chen, X. Su, Q. Fu, H. Lv, Z. He, Z. Cui, Z. Cong, X. Dai, WSi_2 modified HfB_2-SiC coating: microstructure and ablation resistance, J. Eur. Ceram. Soc. 43 (2023) 6746–6757, https://doi.org/10.1016/j.jeurceramsoc.2023.07.070.

[45] D. Hu, Q. Fu, B. Liu, L. Zhou, J. Sun, Multi-layered structural designs of $MoSi_2$/mullite anti-oxidation coating for SiC-coated C/C composites, Surf. Coat. Technol. 409 (2021) 126901, https://doi.org/10.1016/j.surfcoat.2021.126901.

[46] Y.Q. Wang, L.X. Guo, Y.Y. Zhang, X.M. Zhang, H.K. Ou, J. Sun, Ablation behaviors and mechanism of ZrC-SiC-Si/SiC-Si double-layered coatings on C/C composite under plasma flame at 3000 °C, Corros. Sci. 218 (2023) 111200, https://doi.org/10.1016/j.corsci.2023.111200.

[47] T. Li, Y.L. Zhang, Y.Q. Fu, J. Sun, J. Li, Siliconization elimination for SiC coated C/C composites by a pyrolytic carbon coating and the consequent improvement of the mechanical property and oxidation resistances, J. Eur. Ceram. Soc. 41 (2021) 5046–5055, https://doi.org/10.1016/j.jeurceramsoc.2021.04.008.

[48] L. Wang, W.G. Jiang, X.W. Li, J.S. Dong, W. Zheng, H. Feng, L.H. Lou, Effect of surface roughness on the oxidation behavior of a directionally solidified Ni-based superalloy at 1100 °C, Acta Metall. Sin. Engl. 28 (2015) 381–385, https://doi.org/10.1007/s40195-015-0211-2.

[49] N. Hakimi, P. Song, T. Huma, D. Hanifi, D. Bakhshyar, W. Abdul Ghafar, T. Huang, Investigations on oxidation behavior of free-standing CoNiCrAlYHf coating with different surface roughness at 1050 °C, Materials 16 (2023) 4282, https://doi.org/10.3390/ma16124282.

[50] Z. Liao, Y. Wu, H. Yuan, Influences of surface roughness on three dimensional stress concentration factor and fatigue life, China mech, Eng. 26 (2015) 147–151, https://doi.org/10.3969/j.issn.1004-132X.2015.02.002.

[51] B.N.J. Persson, Surface roughness-induced stress concentration, Tribol. Lett. 71 (2023) 68, https://doi.org/10.1007/s11249-023-01741-4.

[52] P. Wang, H. Li, J.a. Kong, R. Yuan, Y. Zhang, A WSi_2-HfB_2-SiC coating for ultralong-time anti-oxidation at 1973 K, Corros. Sci. 159 (2019) 108119, https://doi.org/10.1016/j.corsci.2019.108119.

[53] X. Zhu, Y. Zhang, J. Zhang, T. Li, W. Xie, P. Zhang, H. Li, A compound glass coating with micro-pores to protect SiC-coated C/C composites against oxidation at 1773 K and 1973 K, Corros. Sci. 195 (2022) 109983, https://doi.org/10.1016/j.corsci.2021.109983.

[54] X. Zhu, Y. Zhang, X. Qiang, J. Zhang, Y. Su, T. Li, An oxidation protective coating prepared by SiC densifying HfB_2-SiC skeleton for SiC-coated C/C composites at 1473, 1773, and 1973 K, Corros. Sci. 207 (2022) 110559, https://doi.org/10.1016/j.corsci.2022.110559.

[55] P. Zhang, Q. Fu, C. Cheng, X. Zhu, J. Huang, J. Zhang, W. Li, Comparing oxidation behaviors at 1773 K and 1973 K of HfB_2-$MoSi_2$/SiC-Si coating prepared by a combination method of pack cementation, slurry painting and in-situ synthesis, Surf. Coat. Technol. 403 (2020) 126418, https://doi.org/10.1016/j.surfcoat.2020.126418.

[56] P. Zhang, C. Cheng, B. Liu, W. Xie, X. Zhu, J. Zhang, Q. Fu, Multicomponent $(Hf_{0.25}Zr_{0.25}Ti_{0.25}Cr_{0.25})B_2$ ceramic modified SiC-Si composite coatings: in-situ synthesis and high-temperature oxidation behavior, Ceram. Int. 48 (2022) 12608–12624, https://doi.org/10.1016/j.ceramint.2022.01.129.

[57] M. Zhang, D. Hu, Q. Fu, Ablation resistant behavior of silicide modified HfB_2-SiC coating on graphite by spark plasma sintering: role of $MeSi_2$ addition, J. Eur. Ceram. Soc. 44 (2024) 6286–6297, https://doi.org/10.1016/j.jeurceramsoc.2024.04.005.

[58] Y. Zeng, J. Zhang, J. Hou, Y. Wang, H. Li, Improved oxidation and thermal shock resistance of SiC-Si coating with a SiCw/PyC network structure toughened buffer layer, Surf. Coat. Technol. 479 (2024) 130522, https://doi.org/10.1016/j.surfcoat.2024.130522.

[59] J. Zhang, J. Hou, L. Zhou, W. Ding, Q. Fu, $TaSi_2$-modified HfB_2-SiC coating: preparation and ablation behavior, J. Am. Ceram. Soc. 107 (2024) 461–474, https://doi.org/10.1111/jace.19407.

[60] X.F. Zhu, C.Y. Ou, T. Li, Y.L. Zhang, J.S. Lv, R.C. Chen, $HfSi_2$-HfB_2-SiC coating prepared at low temperature to protect SiC-coated C/C composites against oxidation at 1473-1973 K, Ceram. Int. 50 (2024) 13490–13499, https://doi.org/10.1016/j.ceramint.2024.01.261.

[61] G. Chen, Y. Zhang, P. Zhang, Y. Fu, W. Gai, J.a. Kong, Improvement of SiC/PyC coating on mechanical and anti-oxidation properties through biomimetic laminated structure design, Corros. Sci. 209 (2022) 110721, https://doi.org/10.1016/j.corsci.2022.110721.

[62] D. Hu, Q.G. Fu, L. Zhou, B. Liu, J. Sun, Crack development behavior in thermally sprayed anti-oxidation coating under repeated thermal-oxygen coupling environment, Ceram. Int. 47 (2021) 15328–15336, https://doi.org/10.1016/j.ceramint.2021.02.098.

[63] R.S. Lu, J. Yang, J. Wang, R.Z. Wang, V. Shlyannikov, X.C. Zhang, S.T. Tu, Probabilistic damage tolerance assessment method based on the multi-scale crack growth model, Eng. Fract. Mech. 285 (2023) 109297, https://doi.org/10.1016/j.engfracmech.2023.109297.

[64] Y. Wang, C. Wang, Y. You, W. Cheng, M. Dong, Z. Zhu, J. Liu, L. Wang, X. Zhang, Y. Wang, Thermal stress analysis of optimized functionally graded coatings during crack propagation based on finite element simulation, Surf. Coat. Technol. 463 (2023) 129535, https://doi.org/10.1016/j.surfcoat.2023.129535.

[65] Q. Fu, P. Zhang, L. Zhuang, L. Zhou, J. Zhang, J. Wang, X. Hou, R. Riedel, H. Li, Micro/nano multiscale reinforcing strategies toward extreme high-temperature applications: take carbon/carbon composites and their coatings as the examples, J. Mater. Sci. Technol. 96 (2022) 31–68, https://doi.org/10.1016/j.jmst.2021.03.076.

[66] L. Yang, X. Xiao, L. Liu, J. Luo, K. Jiang, X. Han, C. Zhao, J. Zhang, G. Wang, Dynamic oxidation mechanism of carbon fiber reinforced SiC matrix composite in high-enthalpy and high-speed plasmas, J. Adv. Ceram. 11 (2022) 365–377, https://doi.org/10.1016/j.jeurceramsoc.2021.03.064.

[67] D.R. Mumm, A.G. Evans, On the role of imperfections in the failure of a thermal barrier coating made by electron beam deposition, Acta Mater. 48 (2000) 1815–1827, https://doi.org/10.1016/S1359-6454(99)00473-5.
[68] X.R. Ren, W.-g. Wang, K. Sun, Y.W. Hu, L.H. Xu, P.Z. Feng, Preparation of $MoSi_2$-modified HfB_2-SiC ultra high temperature ceramic anti-oxidation coatings by liquid phase sintering, Carbon 197 (2022) 581, https://doi.org/10.1016/S1872-5805(21)60060-4.
[69] S. He, Y. Liu, Z. Ma, S. Zhu, L. Liu, G. Mu, Y. Li, Study on anti-ablation properties of HfB_2-$TaSi_2$ coatings prepared by atmospheric plasma spraying, J. Alloys Compd. 999 (2024) 175069, https://doi.org/10.1016/j.jallcom.2024.175069.